Geostrophically Constrained Flow of Warm Subsurface Waters Into Geometrically Complex Ice Shelf Cavities

G. Finucane [1]and A. L. Stewart [1]

[1]Department of Atmospheric and Oceanic Sciences, University of California, Los Angeles, California, USA

Contents of this file

1. Text S1 to S3
2. Tables S1 to S3
3. Figures S1 to S15

Text S1. Topological definition of HUB.

The main text provides a qualitative definition and visual illustration of the Highest Unconnected isoBath (HUB), which we use to identify the bathymetric constraints on warm water inflows into ice shelf cavities. Here we provide a more rigorous topological defintion for clarity.

Given a continuous function of elevation $Z(x, y) : \mathrm{C} \subset \mathbb{R}^2 \rightarrow \mathrm{D} \subset \mathbb{R}$ And given a subset of points $\mathrm{O} \subset \mathbb{C}$ which are designated open ocean points. The HUB for any point

$x \in$ C is the greatest z_{HUB} such that x is not path connected to any points in O in the set $Z^{-1}((-\infty, z_{\mathrm{HUB}}))$.

A topological space (X, τ) is said to be path-connected (or pathwise connected) if for each pair of (distinct) points a and b of X there exists a continuous mapping $f : [0, 1] \to (X, \tau)$, such that $f(0) = a$ and $f(1) = b$. The mapping f is said to be a path joining a to b. (Definition from "Topology Without Tears" Morris 2020).

Text S2. Additional information on the model configuration

The text in this section provides additional information on the model configuration in the interest of reproducibility. The text below summarizes salient model configuration and parameter choices, but is not exhaustive. For any details of the model configuration that are not covered here, the reader is referred to the model configuration code, a link to which is provided in the main text.

The MITgcm model we use solves the hydrostatic Boussinesq equations to evolve the state of the ocean . It uses the non-linear equation of state of McDougall, Jackett, Wright, and Feistel (2003), which is abbreviated as "MDJWF" in the MITgcm model code.

Along the northern and eastern boundaries we prescribe the temperature and salinity using an open boundary condition with a sponge layer and range of restoring time scales (see Table S3). The hydrography at the boundaries is comprised of three distinct water masses: the surface water mass has a salinity of 34.15 g/kg and a temperature of -1.8 °C; below it the CDW temperature maximum has a salinity of 34.67 g/kg and a temperature of 1 °C; at the very bottom the salinity drops to 34.65 g/kg and the temperature to -0.5 °C. The properties of each water mass was selected to approximate various hydrographic

profiles around Antarctica from the WOA climatology (Boyer et al., 2018). In the top 75m of the forcing profile the temperature and salinity are constant and equal to that of surface water mass to mimic a surface mixed layer. Below the mixed layer, the temperature and salinity are interpolated using a piecewise-cubic polynomial to reach the CDW temperature maximum at a depth $z = -H_{\max}$, which varies between simulations as discussed in the main text, and to reach the bottom water properties at the bottom of the model domain. This temperature/salinity profile is also used to restore the stratification along the eastern boundary, except the depth of the CDW temperature maximum deepens linearly toward the shelf break, simulating the presence of an Antarctic Slope Front (Thompson et al., 2018). The western boundary is an open boundary with an Orlanski radiation condition.

The flow in our simulations is also subject to the effect of unresolved sub-gridscale turbulence, which is parameterized in the following ways: First, we impose a quadratic frictional stress at the sea floor and at the based of the ice, with non-dimensional coefficient $C_d = 2.0 \times 10^{-3}$. Small-scale energy and enstrophy are controlled via a biharmonic Smagorinsky viscosity with a dimensionless coefficient of $A_{\text{Smag}} = 4$ (Griffies & Hallberg, 2000), accompanied by a Laplacian vertical viscosity of $A_r = 3 \times 10^{-4}\,\text{m}^2/s$. The MITgcm implementation of the KPP mixing parameterization is used. In this version of the MITgcm model (65u), the KPP parameterization creates a region of relatively large vertical diffusion ($\kappa_r \sim 0.005\text{m}^2/\text{s}$) that is typically one grid cell thick just under the ice shelf base. This region of large diffusion mimics the high mixing close to the ice base due to the buoyant melt plume (Lazeroms et al., 2018), which we are unable to resolve on the

vertical scale of our model. This high diffusion region leads to a more realistic cavity circulation by preventing spurious numerical double diffusion at the ice face (not shown).

We use the MITgcm SHELFICE package with the simple boundary layer mixing parameterization enabled (Losch, 2008).

All cavity geometries exhibited a similar pattern of approximately steady circulation and melt that is consistent with previous studies: A warm cross-shelf bottom water current is diverted into the cavity along its eastern wall, circulates anticyclonically and exits along the westward wall (Fig. 2(d)). The southward extent and exact path of this anticyclonic current is altered by each cavity geometry's random bathymetry. This circulation pattern is qualitatively similar to previous idealized ice shelf cavity studies (e.g. Zhao et al., 2019; De Rydt et al., 2014; Rosier et al., 2023). The melt is strongest along the grounding line where warm water first makes contact with the shelf, and then along the western wall due to the resulting melt plume (see the melt rates of the reference case (Fig. S10(b)) for example). This melt pattern is also qualitatively similar to previous idealized ice shelf cavity simulations (see De Rydt et al. (2014); Rosier et al. (2023)). The cross-shelf temperature structure Fig. 2(b) shows that isosurfaces of temperature are deflected downwards along the bottom of the ice shelf face which is in agreement with previous idealized modeling studies (e.g. see Fig. 5 in De Rydt et al., 2014) and regional models see (e.g. see Fig. 2 in Nakayama et al., 2019), and conforms to the assumptions of our theory for the geostrophically-constrained transport (Section 2).

Text S3. Application of the theory to observations

Here we provide additional detail on the calculation of the parameters for our theory from the observed geometry of the near-Antarctic sea floor and the climatological hydrography over the continental slope.

To compute the terms in (6), for each point along a given ice shelf grounding line we require a corresponding hydrographic profile that is representative of conditions at the location of the HUB (*c.f.* Fig. 1). We draw these hydrographic profiles from the WOA casts just offshore of the continental shelf, approximately along the 1500m isobath that encircles Antarctica (Fig. S1), because parts of the Antarctic continental shelf have never been directly measured (See Fig. 2 of Haumann et al. (2020)). A caveat to this approach is that processes occurring across the Antarctic slope front (Thompson et al., 2018) and the continental shelf (Klinck & Dinniman, 2010; Moorman et al., 2023) may lead to hydrographic variations between the continental shelf break and the fronts of the ice shelf cavities.

We select the WOA hydrographic profile closest to the HUB for each grounding line point by combining the HUB and a breadth first search. Briefly, we first calculate the HUB, which we denote as z_{HUB}, for each grounding line point, which we denote by the vector location $\mathbf{x}_{\mathrm{GL}}$. We then seek the shortest path from $\mathbf{x} = \mathbf{x}_{\mathrm{GL}}$ to the 1500m isobath that ascends no shallower than just above z_{HUB}, *i.e.* we insist that the path follow the deepest isobath connecting $\mathbf{x}_{\mathrm{GL}}$ with the open ocean. Mathematically, this corresponds to conducting a breadth-first search that starts at $\mathbf{x} = \mathbf{x}_{\mathrm{GL}}$, that is restricted to depths satisfying $z < z_{HUB} + \epsilon$ (where ϵ is arbitrarily chosen to be 5m), and that terminates upon reaching any point $\mathbf{x} = \mathbf{x}_{1500}$ along the circum-Antarctic 1500m isobath. We then use the

geographically closest WOA cast to $\mathbf{x}_{1500}$ to compute the hydrographic parameters for our theory. For example, Fig. 3(a) shows the selected WOA cast that is selected by our algorithm for a point on the grounding line of the Amery ice shelf.

Once we have found the WOA hydrographic profile for each grounding line point $\mathbf{x}_{\mathrm{GL}}$, we compute the hydrographic parameters for our theory as follows: We calculate $(\theta_{CDW} - \theta_{surf})$ as the average temperature above freezing between z_{HUB} and $z_{HUB}+100\,\mathrm{m}$, in order to mitigate observational noise (see Fig. 3(b)). In order to approximate the thickness of the CDW layer, H_{CDW}, we first estimate the depth of the pycnocline that separates surface waters from CDW. To find the depth of the pycnocline (H_{pyc}) we first smooth each density profile using a moving average with a window of 50 meters, calculate $\frac{\delta\rho}{\delta z}(z)$, and compute the average depth of all points with a $-\frac{\delta\rho}{\delta z}(z)$ above the 85th percentile. We find that this consistently captures the depth of the pycnocline while being relatively insensitive to local maxima of the density gradient elsewhere in the hydrographic profile. We then average the density 50 m above and below $z = -H_{pyc}$ to find σ_{CDW} and σ_{surf}, and thus calculate g'_{out}.

To determine a single ice shelf slope $\overline{s_{ice}}$ for each ice shelf cavity we first section the ice draft data from Bedmachine (Morlighem, 2020) using the ice shelf boundaries from MEASURES (Mouginot et al., 2017) datasets. We then compute the least squares fit of a plane ($a\mathbf{x} + b\mathbf{y} + c = z$) to the draft of the largest continuous region of the ice shelf. We then define $s_{\mathrm{ice}} = \sqrt{a^2 + b^2}$ such that slope is the same regardless of the orientation of the plane.

We make this choice because it calculates a slope most similar to the linear slope in our idealized model configuration and is insensitive to small scale local changes in ice thickness like ridges in the ice. **Note:** we exclude at this step ice shelves with less than 100 continuous points in Bedmachine2.

The parameter α is 1.25 times larger in the modeling results when compared to the observational results. One source of this difference could be the fact that in our observational estimate we use the W_0 length scale derived from our modeling experiments, but, that length scale may be different in real ice shelves. It also may be the case that the slightly different methods we use to calculate Eq. 5 in observations compared to the models yields a factor of 1.25 difference.

Table S1.

Experiment Name	Shelf depth (m)	Random bathymetry seed	Random bathymetry amplitude (m)	Cavity depth and shelf depth difference (m)	Cavity width (m)	Ice shelf northward extent (m)
ref	650	32	0	-300	150	150
y100	650	64	250	-300	150	**100**
y250	650	64	250	-300	150	**250**
d500	**500**	16	200	-300	150	150
d600	**600**	16	200	-300	150	150
d700	**700**	16	200	-300	150	150
w50	650	32	250	-300	**50**	150
w100	650	32	250	-300	**100**	150
w250	650	32	250	-300	**250**	150
s0	900	22	250	**0**	150	150
s150	900	22	250	**150**	150	150
s300	900	22	250	**300**	150	150

Table S2.

Symbol	Definition
C_p	Specific heat of water
f	Coriolis parameter
g'_in	Reduced gravity inside of cavity
g'_out	Reduced gravity outside of cavity
H_CDW	Thickness of CDW at deepest entrance point to cavity
h_CDW	Thickness of CDW
I_f	Latent heat of melt
L	Length of Cavity (perpendicular to grounding line)
s_CDW	Slope of interface between CDW and surface waters
s_ice	Slope of ice shelf face
T	Transport of CDW into the cavity
u_CDW	velocity of CDW layer
W	Width of ice shelf cavity (parallel to grounding line)
W_0	Melt length scale
ρ_0	Reference density of water
ρ_i	Reference density of ice
θ_CDW	Potential temperature of CDW layer
θ_surf	Potential temperature of surface layer

Table S3.

Param.	Value	Description
L_x	400km	Zonal domain size
L_y	300km	Meridional domain size
H	1500m	Maximum ocean depth
L_r	20km	Sponge thickness
τ_o^{in}	10 days	Inner relaxation timescale for ocean
τ_o^{out}	12 hours	Outer relaxation timescale for ocean
f_0	$-1.3 \times 10^{-4} s^{-1}$	Reference Coriolis parameter
β	$1 \times 10^{-11} (ms)^{-1}$	Rossby parameter
C_d	2×10^{-3}	Quadratic frictional drag coefficient
A_v	$1 \times 10^{-4} m^2 s^{-1}$	Vertical eddy viscosity
Δ_x, Δ_y	2.08 km, 2.0 km	Horizontal grid spacing
Δ_z	2-200 m	Vertical grid spacing
Δ_t	75–175s	Time step

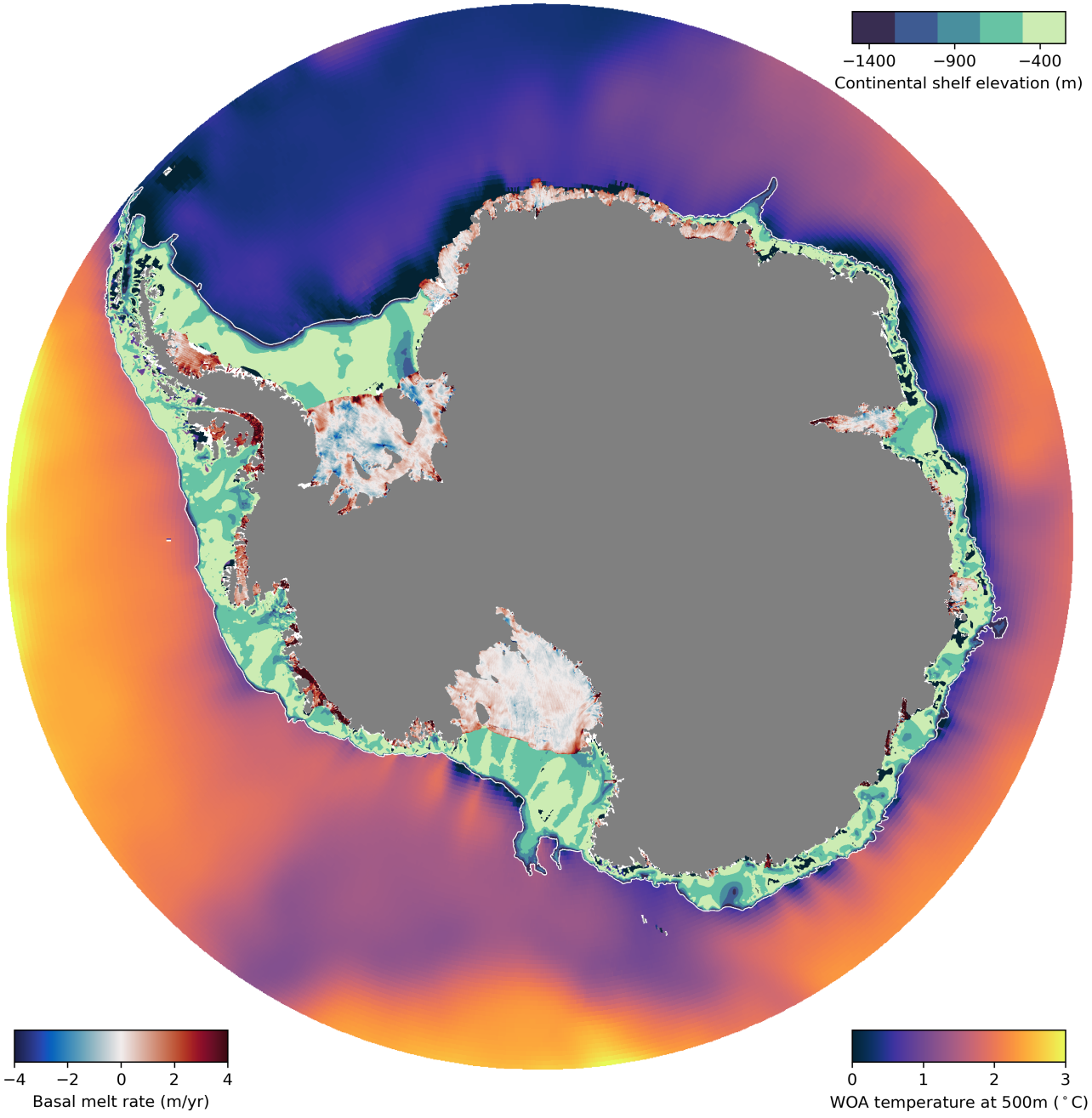

Figure S1. World Ocean Atlas (Boyer et al., 2018) temperatures at a depth of 500 m are plotted for locations with a depth greater than 1500 m. The bathymetry of the continental shelf from BedMachine2 (Morlighem, 2020) is plotted for depths shallower than 1500 m in regions that are not covered by ice shelves. Where there are ice shelves, the satellite derived basal melt rate from Adusumilli et al. (2020) is plotted.

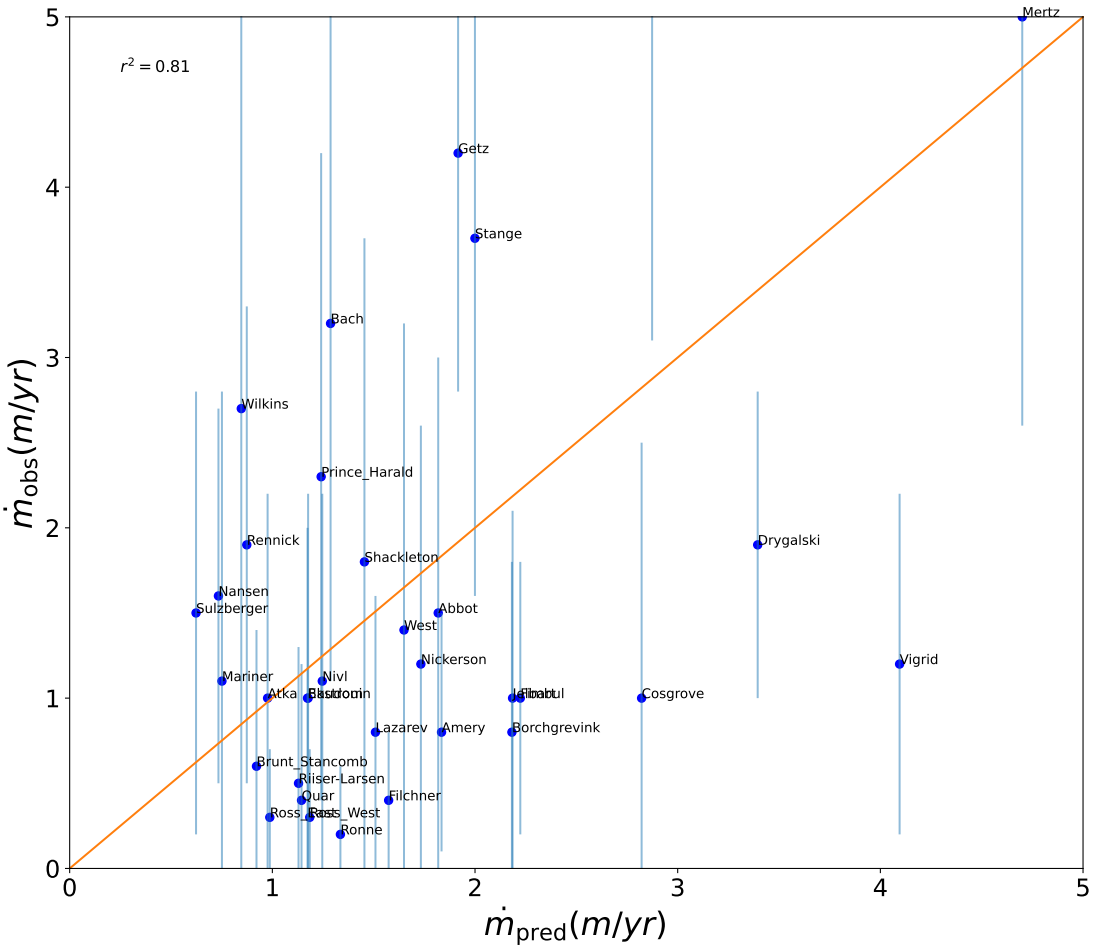

Figure S2. Same as Figure 4c, but zoomed into the bottom left corner where predicted and observed melt rates are low. Error bars are estimates of observational error from Adusumilli et al. (2020)

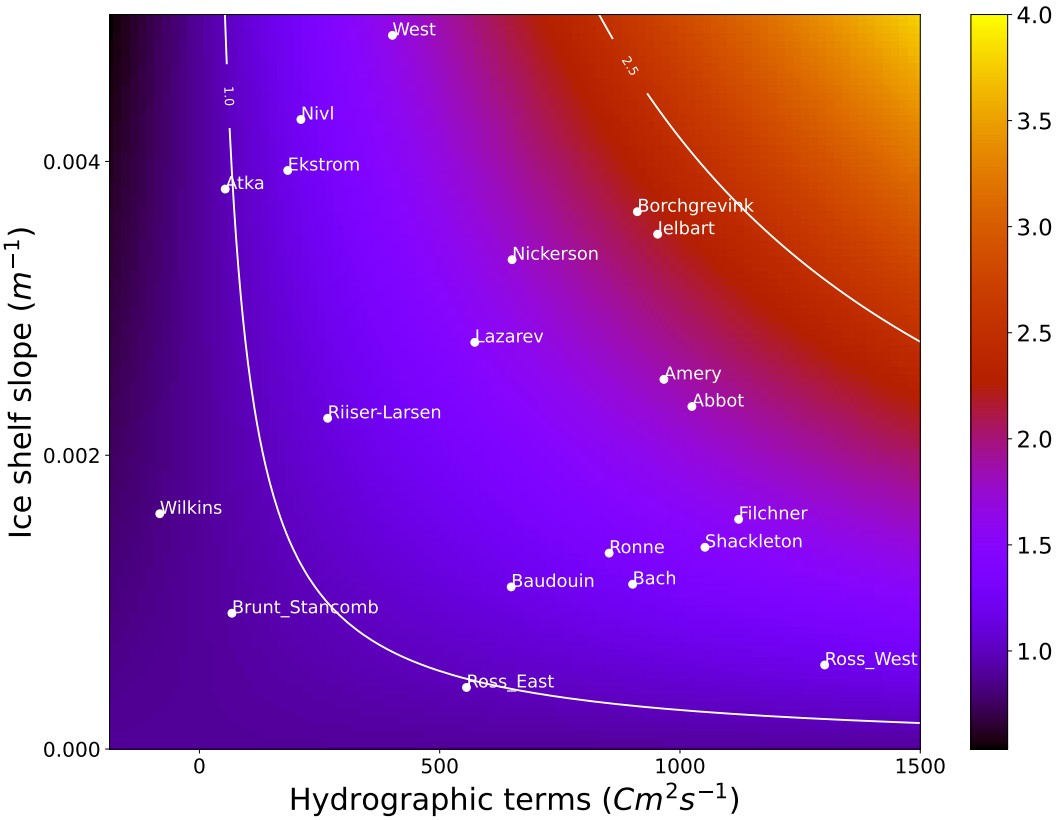

Figure S3. Same as Figure 4d, but zoomed into the bottom left corner where slope and hydrographic terms are low. The color bar magnitude has been changed from Figure 4d to better show differences in predicted melt in this smaller range.

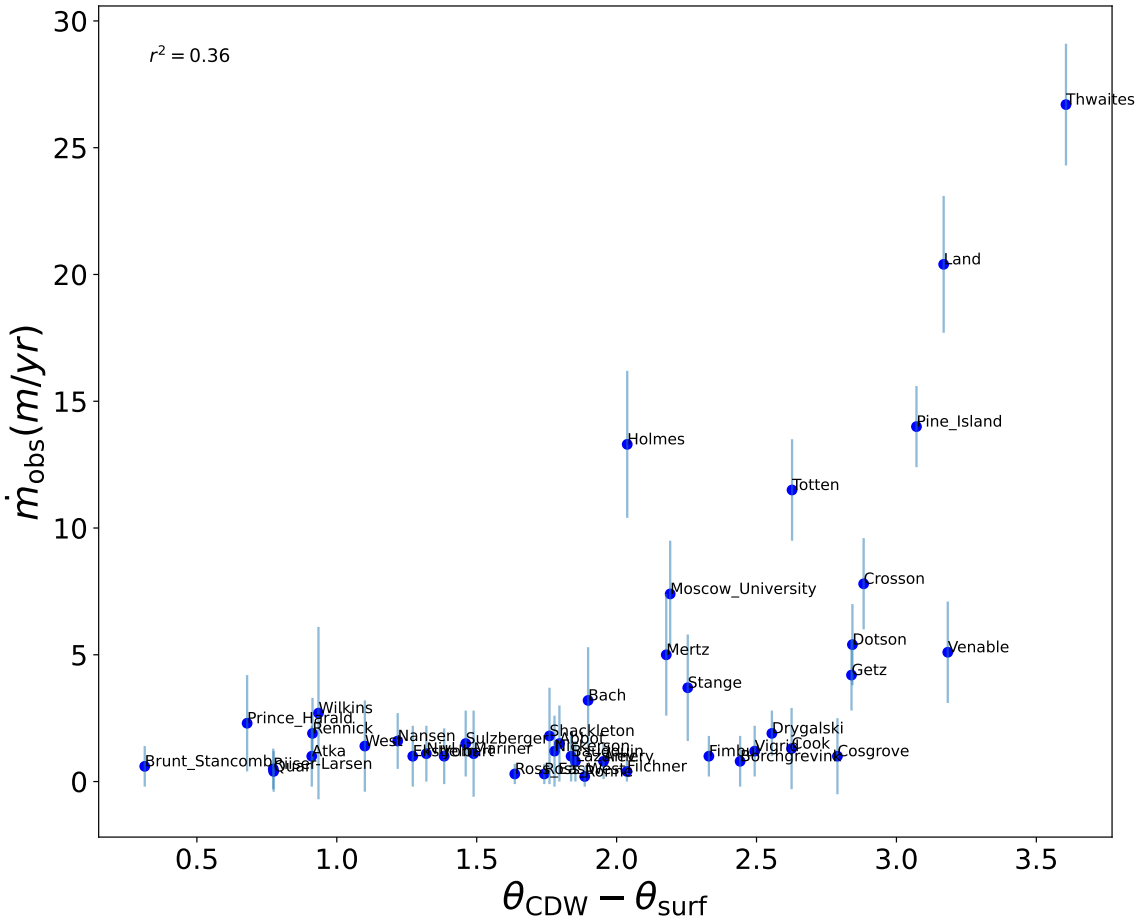

Figure S4. The thermal forcing term from Eq. 5 plotted against observed melt rates from Adusumilli et al. (2020). Error bars are estimates of observational error from Adusumilli et al. (2020).

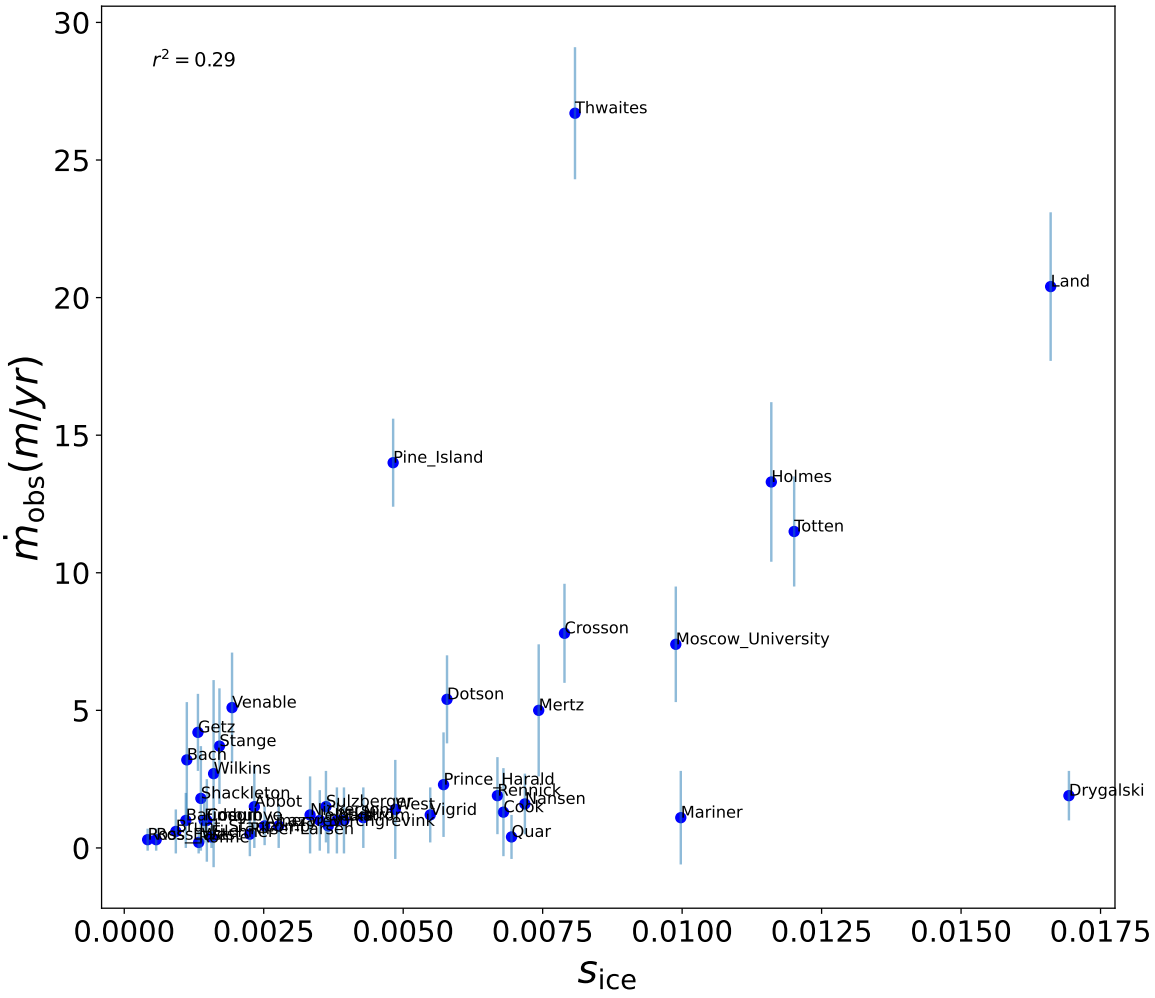

Figure S5. The slope term from Eq. 5 plotted against observed melt rates from Adusumilli et al. (2020). Error bars are estimates of observational error from Adusumilli et al. (2020).

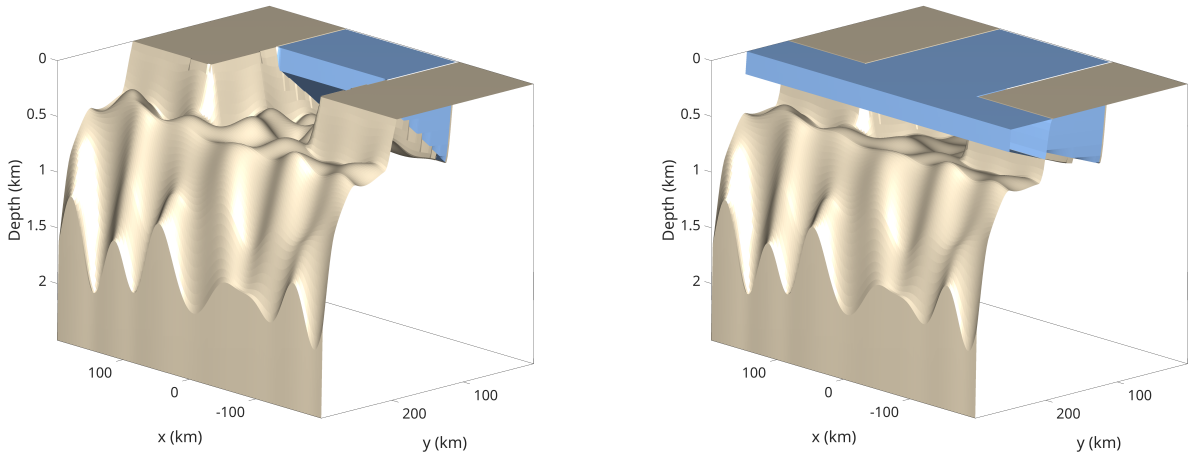

Figure S6. Model geometry of simulations with varying ice shelf extents. On the left, a simulation with an icefront of 100 km (y100). On the right, a simulation with an icefront of 250 km (y250)

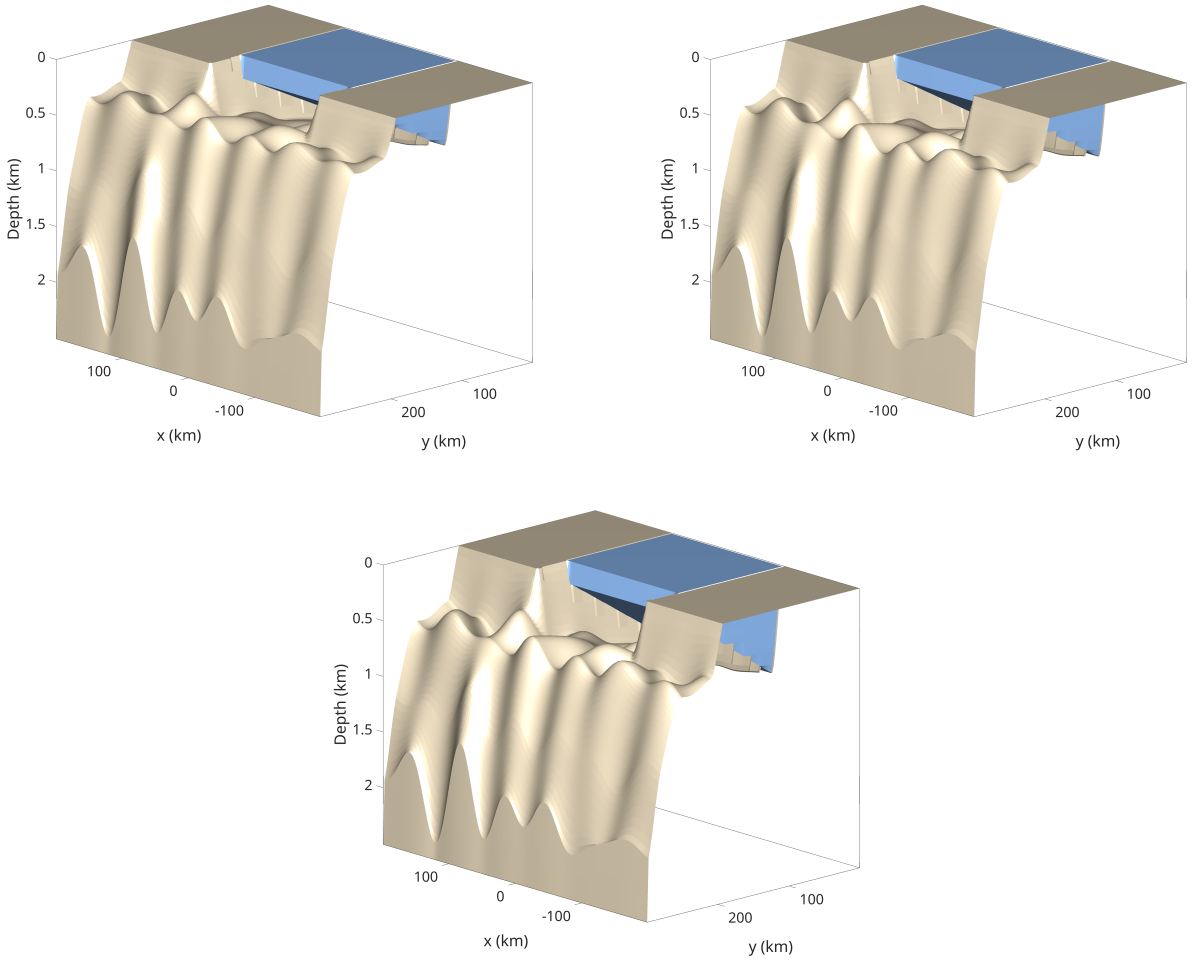

Figure S7. Model geometry of simulations with varying shelf depths. On the top left, a simulation with a depth of 500 m (d500). On the top right, a simulation with a shelf depth of 600 m (d600). On the bottom, a simulation with a shelf depth of 700 m (d700).

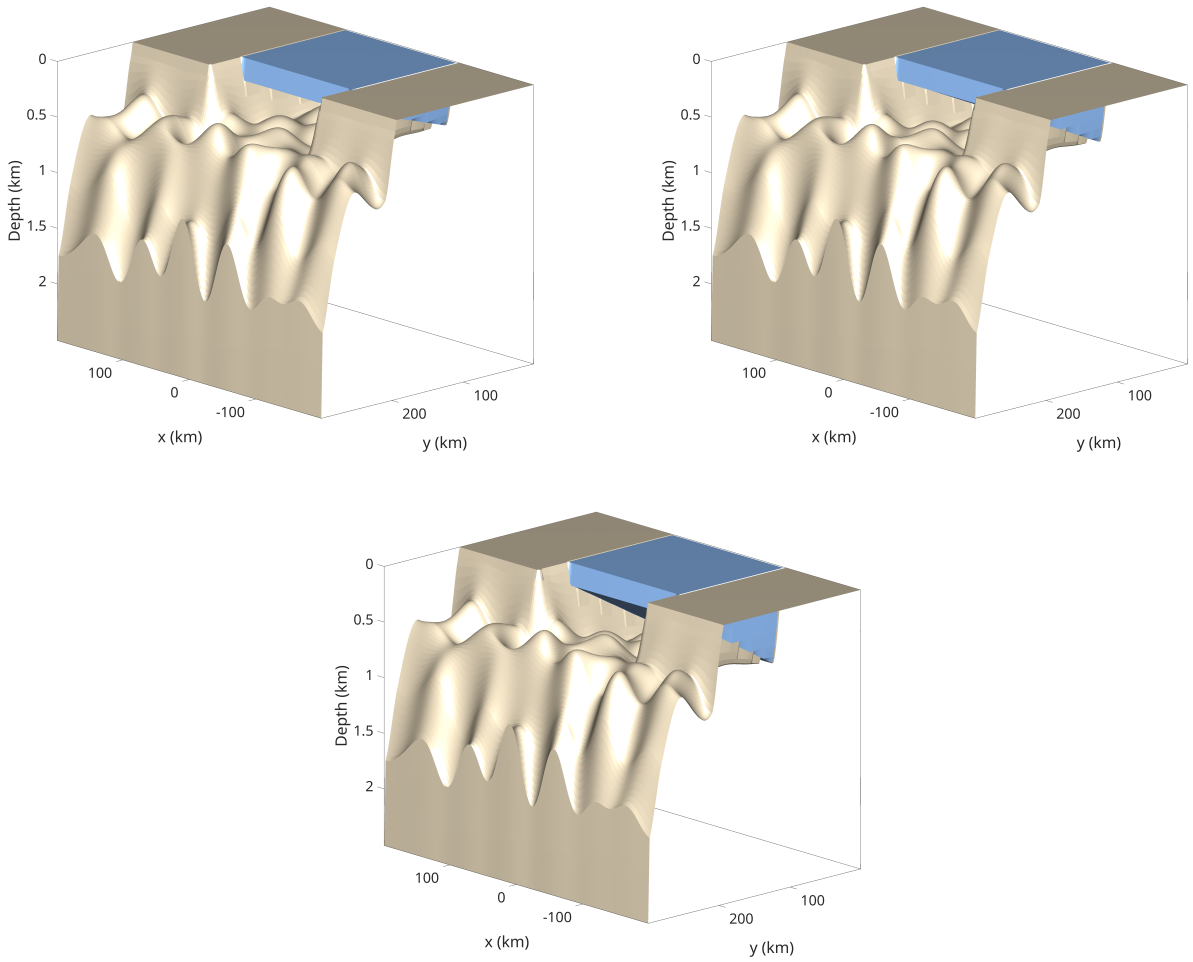

Figure S8. Model geometry of simulations with varying bed slopes. On the top left, a simulation with a continental shelf 300 m deeper than the grounding line (s300). On the top right, a simulation with a continental shelf 150 m deeper than the grounding line (s150). On the bottom, a simulation with a continental shelf 0 m deeper than the grounding line (s0).

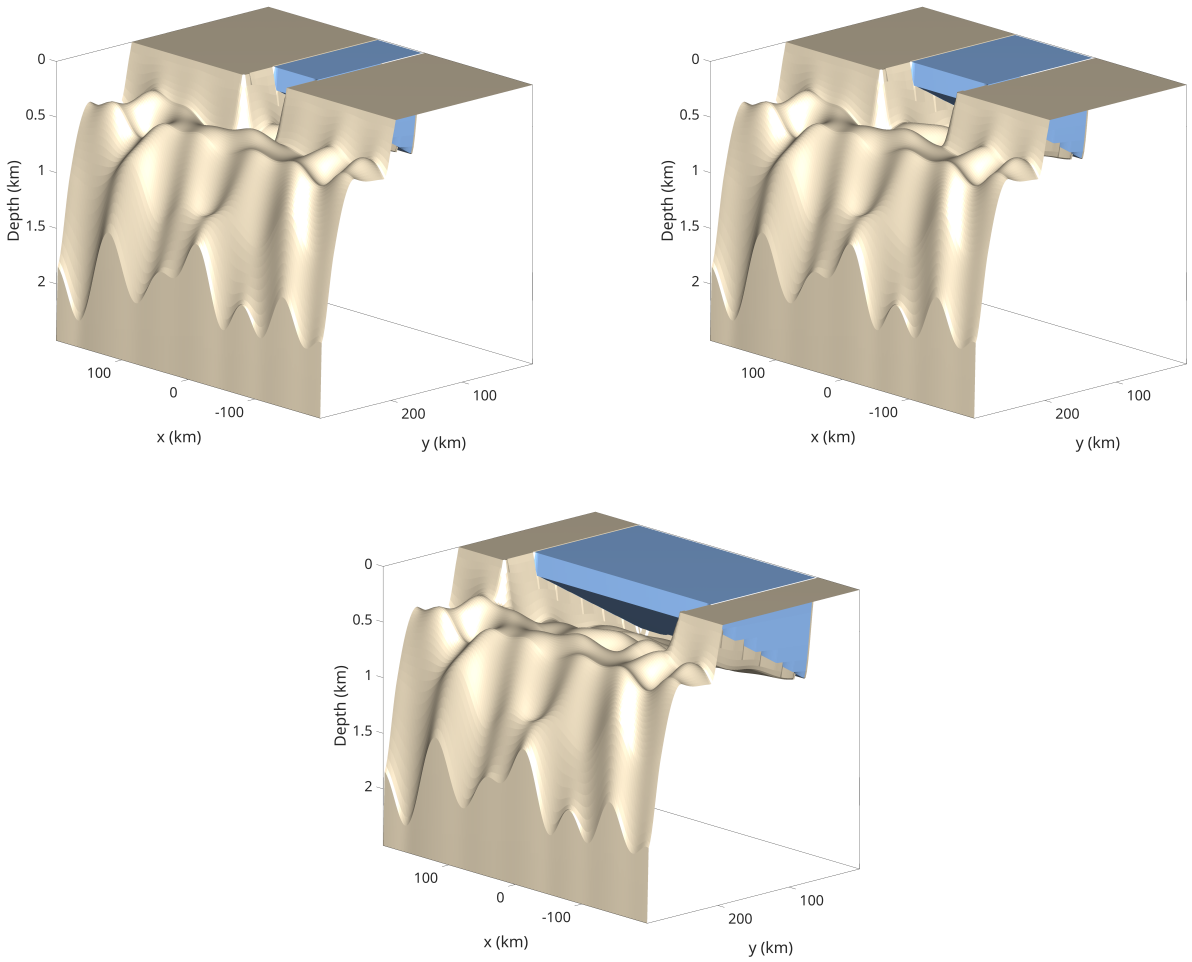

Figure S9. Model geometry of simulations with varying cavity widths. On the top left, a simulation with a continental shelf 50 km wide (w50). On the top right, a simulation with a continental shelf 100 km wide (w100). On the bottom, a simulation with a continental shelf 250 km wide (w250).

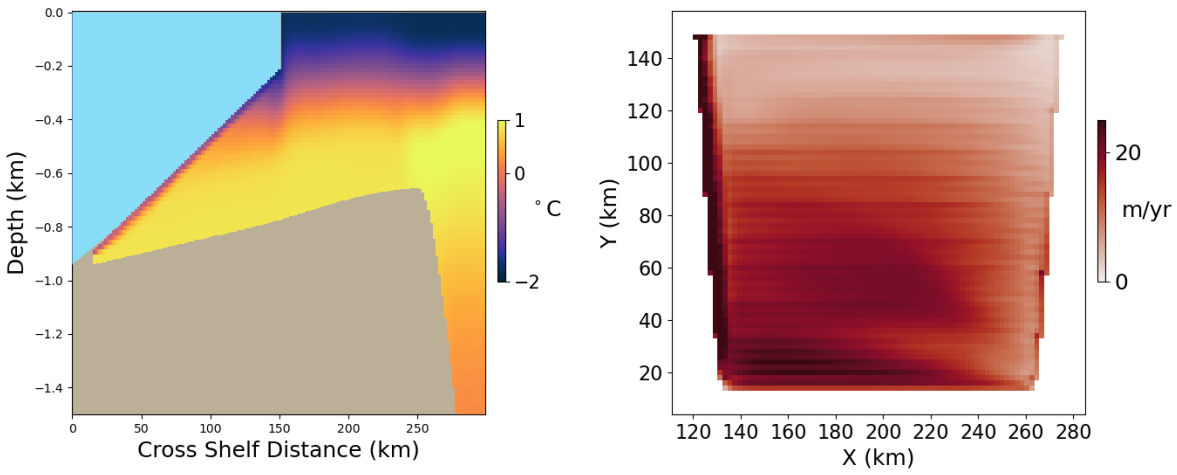

Figure S10. Meridional cross sections of time-average potential temperature (left column) and maps of time-average ice shelf melt in m/yr (right column) from high thermocline model simulations with reference geometry.

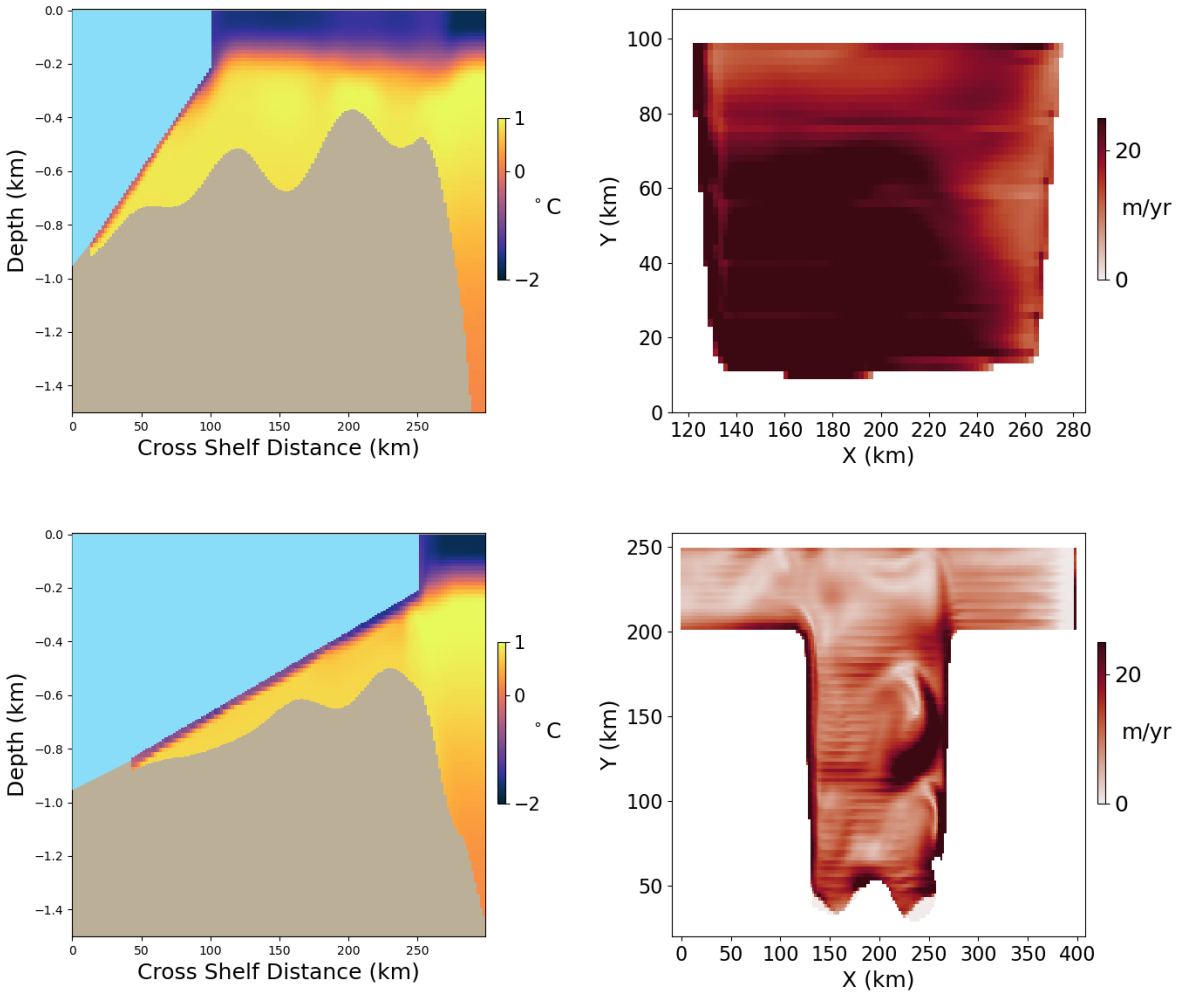

Figure S11. Meridional cross sections of time-average potential temperature (left column) and maps of time-average ice shelf melt in m/yr (right column) from high thermocline model simulations with varying ice shelf extent. At the top a simulation with an icefront of 100 km (y100). On the bottom, a simulation with an icefront of 250 km (y250)

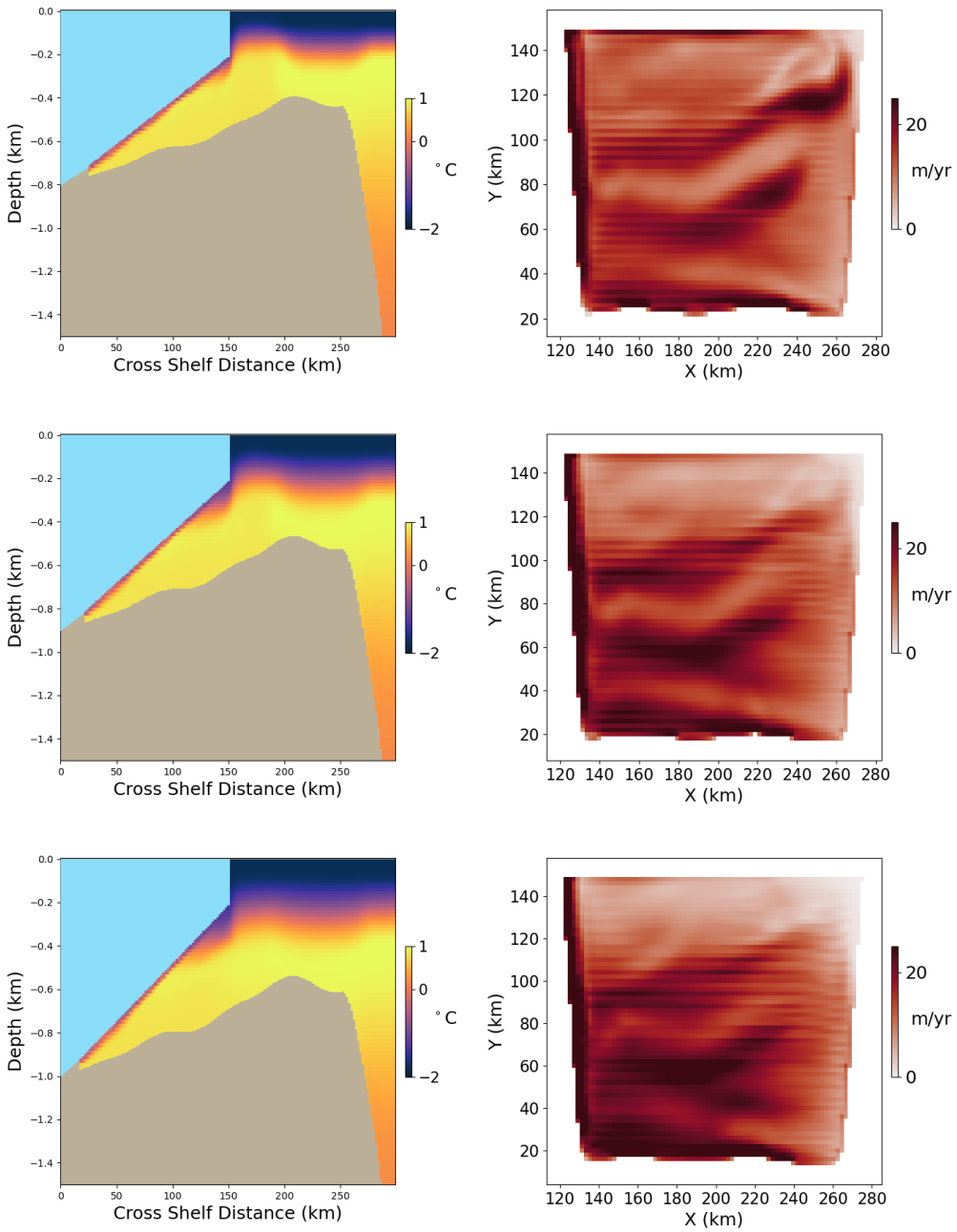

Figure S12. Meridional cross sections of time-average potential temperature (left column) and maps of time-average ice shelf melt in m/yr (right column) from high thermocline model simulations with varying shelf depths. At the top , a simulation with a depth of 500 m (d500). In the middle, a simulation with a shelf depth of 600 m (d600). On the bottom, a simulation with a shelf depth of 700 m (d700).

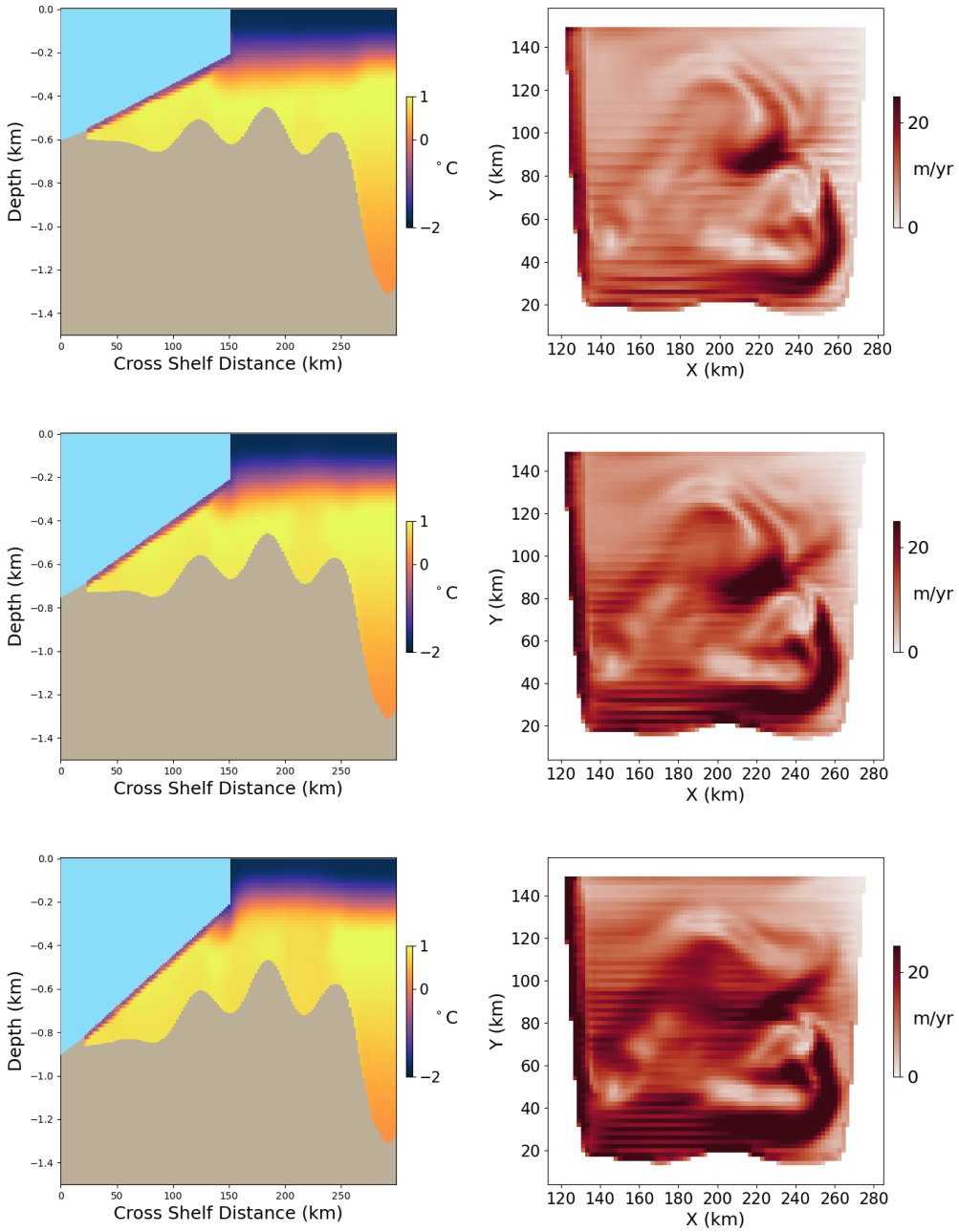

Figure S13. Meridional cross sections of time-average potential temperature (left column) and maps of time-average ice shelf melt in m/yr (right column) from high thermocline model simulations with varying bed slopes. On the top, a simulation with a continental shelf 300 m deeper than the grounding line (s300). In the middle, a simulation with a continental shelf 150 m deeper than the grounding line (s150). On the bottom, a simulation with a continental shelf 0 m deeper than the grounding line (s0).

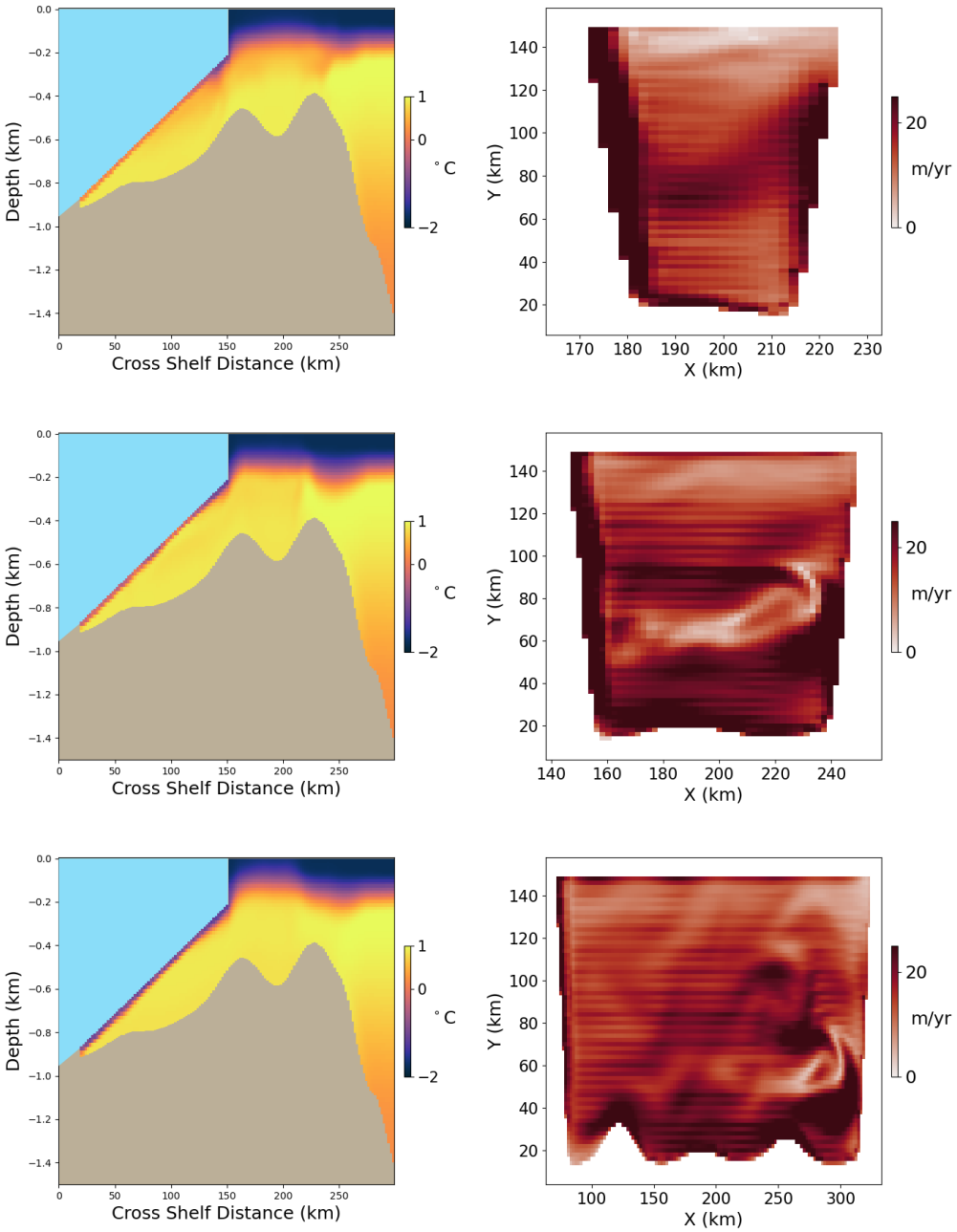

Figure S14. Meridional cross sections of time-average potential temperature (left column) and maps of time-average ice shelf melt in m/yr (right column) from high thermocline model simulations with varying cavity widths. On the top, a simulation with a continental shelf 50 km wide (w50). In the middle, a simulation with a continental shelf 100 km wide (w100). On the bottom, a simulation with a continental shelf 250 km wide (w250).

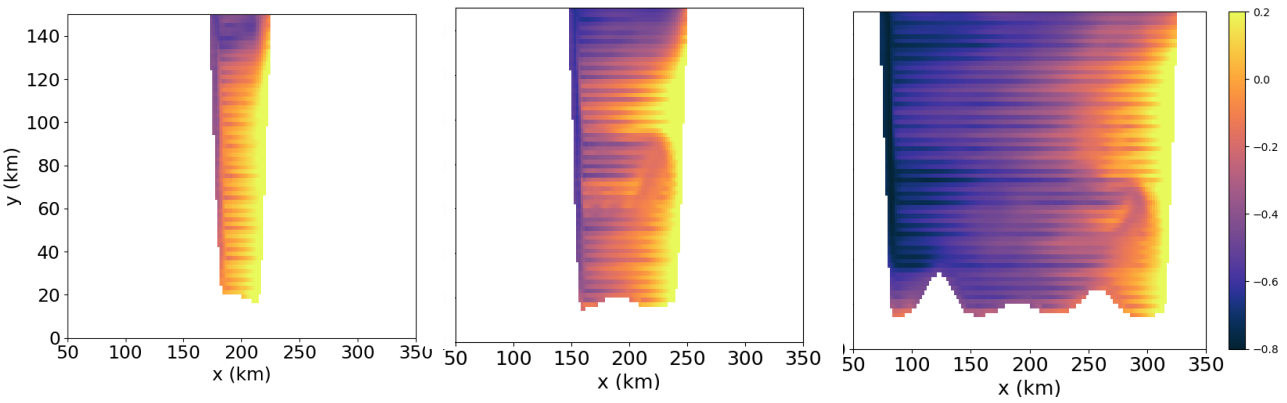

Figure S15. Maps of time average potential temperature directly below ice shelf face in high thermocline simulations with varying widths. On the left, a simulation with a continental shelf 50 km wide (w50). In the middle, a simulation with a continental shelf 100 km wide (w100). On the right, a simulation with a continental shelf 250 km wide (w250).

References

Adusumilli, S., Fricker, H. A., Medley, B., Padman, L., & Siegfried, M. R. (2020). Interannual variations in meltwater input to the Southern Ocean from Antarctic ice shelves. *Nature Geoscience*, *13*(9), 616–620. doi: 10.1038/s41561-020-0616-z

Boyer, T. P., Garcia, H. E., Locarnini, R. A., Zweng, M. M., Mishonov, A. V., Reagan, J. R., ... Smolyar, I. V. (2018). *World ocean atlas 2018.* NOAA National Centers for Environmental Information.

De Rydt, J., Holland, P. R., Dutrieux, P., & Jenkins, A. (2014). Geometric and oceanographic controls on melting beneath Pine Island Glacier. *Journal of Geophysical Research: Oceans*, *119*(4), 2420–2438. doi: 10.1002/2013JC009513

Griffies, S. M., & Hallberg, R. W. (2000). Biharmonic friction with a Smagorinsky-like viscosity for use in large-scale eddy-permitting ocean models. *Mon. Weather Rev.*, *128*(8), 2935–2946.

Haumann, F. A., Moorman, R., Riser, S. C., Smedsrud, L. H., Maksym, T., Wong, A. P. S., ... Sarmiento, J. L. (2020). Supercooled Southern Ocean Waters. *Geophysical Research Letters*, *47*(20), e2020GL090242. doi: 10.1029/2020GL090242

Klinck, J. M., & Dinniman, M. S. (2010). Exchange across the shelf break at high southern latitudes. *Ocean Science*, *6*(2), 513–524. doi: 10.5194/os-6-513-2010

Lazeroms, W. M. J., Jenkins, A., Gudmundsson, G. H., & van de Wal, R. S. W. (2018). Modelling present-day basal melt rates for Antarctic ice shelves using a parametrization of buoyant meltwater plumes. *The Cryosphere*, *12*(1), 49–70. doi: 10.5194/tc-12-49-2018

Losch, M. (2008). Modeling ice shelf cavities in a z coordinate ocean general circulation model.

Journal of Geophysical Research: Oceans, *113*(C8). doi: 10.1029/2007JC004368

McDougall, T. J., Jackett, D. R., Wright, D. G., & Feistel, R. (2003). Accurate and Computationally Efficient Algorithms for Potential Temperature and Density of Seawater. *Journal of Atmospheric and Oceanic Technology*, *20*(5), 730–741. doi: 10.1175/1520-0426(2003)20⟨730:AACEAF⟩2.0.CO;2

Moorman, R., Thompson, A. F., & Wilson, E. A. (2023). Coastal Polynyas Enable Transitions Between High and Low West Antarctic Ice Shelf Melt Rates. *Geophysical Research Letters*, *50*(16), e2023GL104724. doi: 10.1029/2023GL104724

Morlighem, M. (2020). *Measures bedmachine antarctica, version 2.* NASA National Snow and Ice Data Center Distributed Active Archive Center.

Mouginot, J., Scheuchl, B., & Rignot, E. (2017). *Measures antarctic boundaries for ipy 2007-2009 from satellite radar, version 2.* NASA National Snow and Ice Data Center Distributed Active Archive Center.

Nakayama, Y., Manucharyan, G., Zhang, H., Dutrieux, P., Torres, H. S., Klein, P., ... Menemenlis, D. (2019). Pathways of ocean heat towards Pine Island and Thwaites grounding lines. *Scientific Reports*, *9*(1), 16649. doi: 10.1038/s41598-019-53190-6

Rosier, S. H. R., Bull, C. Y. S., Woo, W. L., & Gudmundsson, G. H. (2023). Predicting ocean-induced ice-shelf melt rates using deep learning. *The Cryosphere*, *17*(2), 499–518. doi: 10.5194/tc-17-499-2023

Thompson, A. F., Stewart, A. L., Spence, P., & Heywood, K. J. (2018). The Antarctic Slope Current in a Changing Climate. *Reviews of Geophysics*, *56*(4), 741–770. doi: https://doi.org/10.1029/2018RG000624

Zhao, K. X., Stewart, A. L., & McWilliams, J. C. (2019). Sill-Influenced Exchange Flows in Ice Shelf Cavities. *Journal of Physical Oceanography*, *49*(1), 163–191. doi: 10.1175/JPO-D-18-0076.1